JCB Journal of Cell Biology

REPORT

An amphipathic helix enables septins to sense micrometer-scale membrane curvature

Kevin S. Cannon[1], Benjamin L. Woods[1], John M. Crutchley[1], and Amy S. Gladfelter[1,2]

Cell shape is well described by membrane curvature. Septins are filament-forming, GTP-binding proteins that assemble on positive, micrometer-scale curvatures. Here, we examine the molecular basis of curvature sensing by septins. We show that differences in affinity and the number of binding sites drive curvature-specific adsorption of septins. Moreover, we find septin assembly onto curved membranes is cooperative and show that geometry influences higher-order arrangement of septin filaments. Although septins must form polymers to stay associated with membranes, septin filaments do not have to span micrometers in length to sense curvature, as we find that single-septin complexes have curvature-dependent association rates. We trace this ability to an amphipathic helix (AH) located on the C-terminus of Cdc12. The AH domain is necessary and sufficient for curvature sensing both in vitro and in vivo. These data show that curvature sensing by septins operates at much smaller length scales than the micrometer curvatures being detected.

Introduction

Shape is a fundamental feature in cell biology and can be thought in terms of membrane curvature (Zimmerberg and Kozlov, 2006; Cannon et al., 2017). Cellular membrane curvature is a continuum, spanning nanometer to micrometer scales. How do cells use nanometer-sized components to perceive micrometer-scale changes in shape? Septins are filament-forming, GTP-binding proteins that localize to sites of micrometer-scale membrane curvature from yeast to humans (Field et al., 1996; Pan et al., 2007; Bridges et al., 2016). Examples of curvature-associated localizations include the bud neck in *Saccharomyces cerevisiae* (Byers and Goetsch, 1976; Haarer and Pringle, 1987; Ford and Pringle, 1991), bases of dendritic spines in neurons (Cho et al., 2011), branches in filamentous fungi (Westfall and Momany, 2002; DeMay et al., 2009; Bridges et al., 2016), and the cytokinetic furrow (Spiliotis et al., 2005; Joo et al., 2007; Maddox et al., 2007). At these sites, septins coordinate cell cycle progression (Longtine et al., 2000; Sakchaisri et al., 2004), influence diffusion in the membrane (Clay et al., 2014; Yamada et al., 2016), and act as a scaffold to recruit proteins required for chromosome segregation (Spiliotis et al., 2005) and cytokinesis (Meitinger et al., 2011; Finnigan et al., 2015).

Septins carry out these functions by assembling into heteromeric, rod-shaped, nonpolar complexes that can anneal end-on to polymerize into filaments at the plasma membrane (Field et al., 1996; John et al., 2007; Sirajuddin et al., 2007; Bertin et al., 2008). Budding yeast possesses five mitotic septins that assemble into hetero-octamers in which the terminal subunit is either Cdc11 or Shs1 (Garcia et al., 2011; Khan et al., 2018). Purified recombinant septins from yeast and humans preferentially adsorb onto micrometer curvatures in the absence of any cellular factors (Bridges et al., 2016), indicating that curvature sensing is a conserved feature of the septin cytoskeleton. The mechanism underlying how septins sense micrometer-scale membrane curvature is unclear.

Most of what we know about curvature sensing comes from nanometer-sized molecules interacting with nanometer-scale curvatures. Proteins containing BAR domains and/or amphipathic helices (AHs) use combinations of membrane insertion (Drin and Antonny, 2010), oligomerization, and scaffolding mechanisms (Simunovic et al., 2013, 2015) to either sense or deform the local curvature. Membrane curvature generates lipid-packing defects, providing binding sites for AHs (Hatzakis et al., 2009). Proteins such as α-synuclein (Pranke et al., 2011), Opi1 (Hofbauer et al., 2018), and ArfGAP1 (Drin et al., 2007) use this mechanism to sense curvature. Interestingly, known micrometer-scale curvature sensors including SpoVM (Ramamurthi et al., 2009) and MreB (Ursell et al., 2014; Hussain et al., 2018) contain AHs.

In this study, we investigate the mechanisms of septin curvature sensing. We discovered that septins vary in their affinity for different curvatures, that single septin oligomers bind with different association rates depending on the curvature, and that a conserved AH is both necessary and sufficient for curvature

[1]Department of Biology, University of North Carolina at Chapel Hill, NC; [2]Marine Biological Laboratory, Woods Hole, MA.

Correspondence to Amy S. Gladfelter: amyglad@unc.edu.

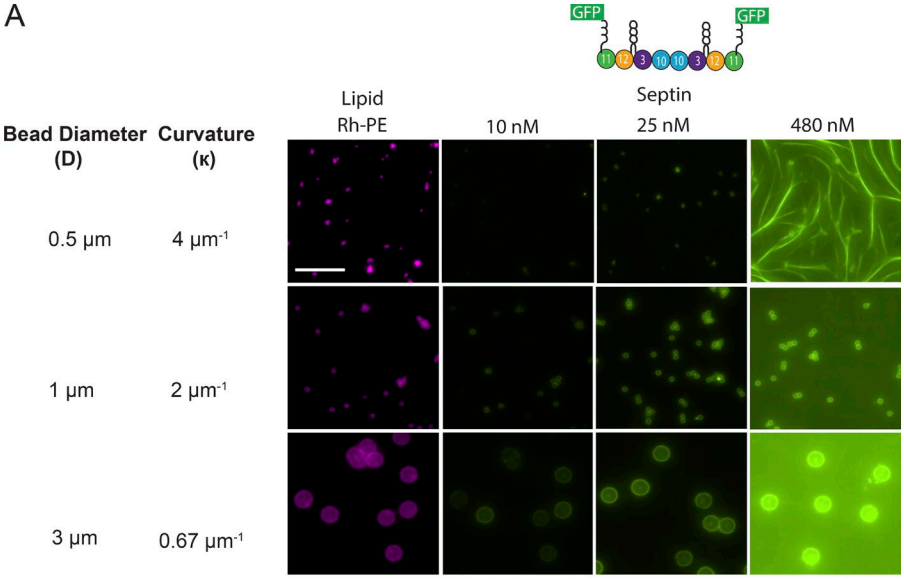

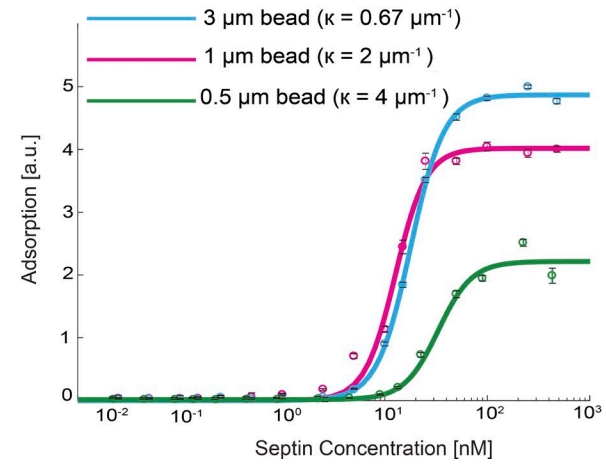

Figure 1. **Septins bind cooperatively to curved membranes, with differences in affinity and maximal binding.** SLBs (75% DOPC, 25% PI, and trace amounts of Rh-PE) were reconstituted on silica beads. Purified septins were added at several concentrations through saturation. **(A)** Representative images are maximum intensity projections. Bar, 10 μm. **(B)** Quantification of septin adsorption at equilibrium onto SLBs of varying curvature. Each data point represents the mean intensity for 98–600 beads. Error bars are SEM, $n = 3$.

sensing by septins. This study provides the first insights into the molecular basis for how septins sense curvature.

Results and discussion

Analysis of septin saturation binding to different curvatures

We first generated saturation binding isotherms from which affinity, maximal binding, and cooperativity can be estimated for septins on different curvatures. We used a minimal reconstitution system consisting of recombinant yeast septin complexes (Cdc11-GFP, Cdc12, Cdc3, and Cdc10) and supported lipid bilayers (SLBs) formed on silica beads of different curvatures (Gopalakrishnan et al., 2009; Bridges et al., 2016). We measured septin binding onto SLB-coated beads at a range of concentrations with different bead sizes using quantitative microscopy. We found that septins have the strongest affinity for 1-μm beads (curvature, $\kappa = 2\ \mu m^{-1}$; K_d 13.5 nM), followed by 3-μm beads ($\kappa = 0.67\ \mu m^{-1}$; K_d 18.5 nM), and 0.5-μm beads ($\kappa = 4\ \mu m^{-1}$; K_d 34.3 nM; Fig. 1 and Table S1). Additionally, the difference in maximal binding capacity is dramatically different for tested bead sizes, indicating that there are curvature-dependent differences in the number of effective binding sites for septins (Fig. 1 and Table S1). This is not due to differences in surface area on different bead sizes, as we normalized for surface area. At high septin concentrations, filaments formed in solution at curvature $\kappa = 4\ \mu m^{-1}$, indicating excess complex is available for polymerization, suggesting the number of binding sites is limiting at this curvature (Fig. 1). Hill coefficients of 2.6 ($\kappa = 4\ \mu m^{-1}$and $\kappa = 0.67\ \mu m^{-1}$) and 2.9 ($\kappa = 2\ \mu m^{-1}$) indicated septin adsorption on all tested membrane curvatures is cooperative, consistent with the observation that some beads are fully bound by septins, whereas others have none.

We predict that affinity is a major driver of curvature sensing at low septin concentrations, and at high concentrations, how dense filaments can arrange on different curvatures becomes important. Collectively, these data suggest that differences in septin affinity and the number of available binding sites can drive preferential assembly of septins onto specific curvatures in a cooperative fashion. Cooperativity in assembly could arise at filament formation, lateral associations between filaments and/or other higher-order structures including layers of filaments.

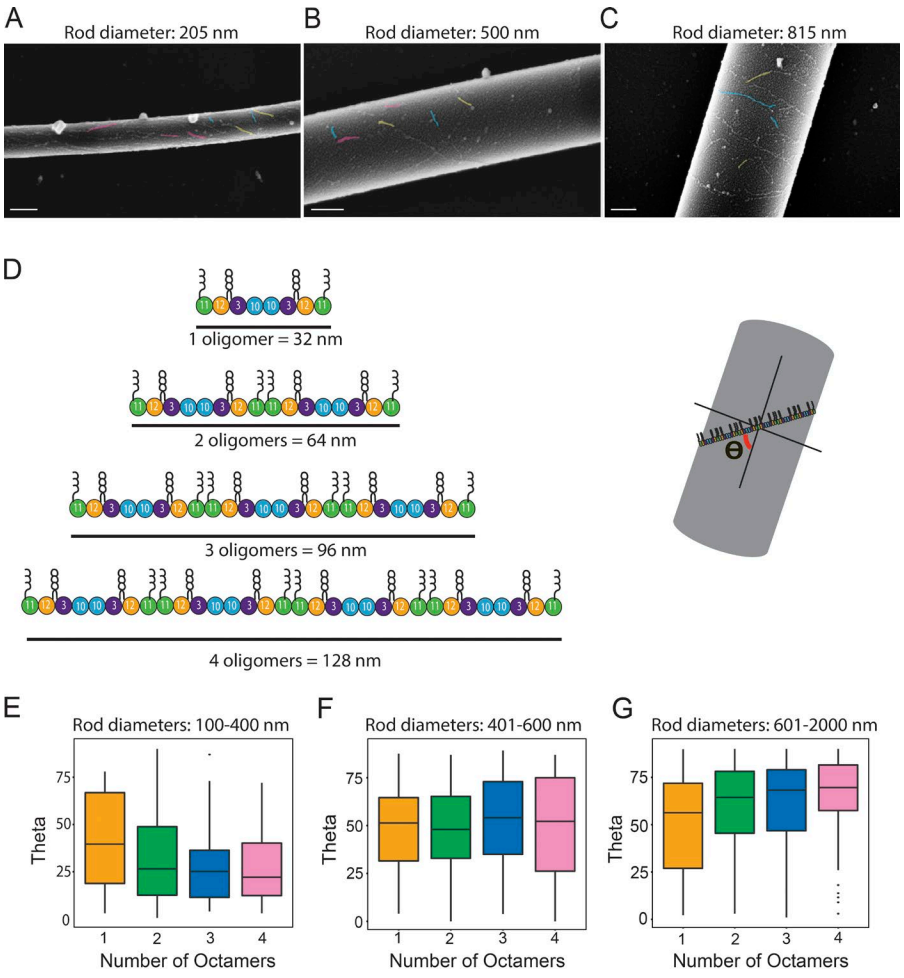

Figure 2. **Septin filament alignment toward the axis of principal curvature is dependent on filament length.** SLBs (75% DOPC, 25% PI, and trace amounts of Rh-PE) were reconstituted on borosilicate rods of different diameters ranging from ∼100 nm to 2,300 nm. **(A–C)** Representative images of septin filament alignment on rods from the three different categories. Bars, 200 nm. A subset of filaments was false colored to depict alignments; pink are parallel to the long axis of curvature; yellow are oriented at ∼45°; blue are aligned to the axis of principal curvature. **(D)** Schematic of septin filament length in terms of the number of octamers and a cartoon depicting how filament orientation relative rod was measured. **(E–G)** Box and whisker plot quantifying septin filament alignment on various rod diameters as a function of filament length binned to three diameter ranges. Black bars represent the median. Error bars are standard deviation. **(E)** 100–400 nm rods. *n* = 23 rods and 193 filaments. **(F)** 401–600 nm rods. *n* = 15 rods and 189 filaments. **(G)** 601–2,000 nm rods. *n* = 24 rods and 491 filaments.

Septin filament orientation is dependent on membrane curvature

To evaluate how cooperativity may arise at the level of polymerization, we asked how long a septin filament must be to align along optimum curvature. We adapted the SLB assay to rods of different diameters to visualize filaments using scanning EM. We scored the length and orientation of filaments on a range of rod diameters binned to three categories (100–400, 401–600, and 601–1,000 nm). For all three categories, we found that single septin octamers (32 nm in length) sampled a variety of orientations as each image is a snapshot at the time of fixation (Fig. 2, E–G, orange boxes; and Table S2). For rod diameters of 600–1,000 nm, filaments 64 nm long tended to align along the axis of principal curvature (Fig. 2 G, green boxes). On rod diameters from 401–600 nm, septin filaments up to 128 nm long (four annealed octamers) had a wide distribution of orientations (Fig. 2 F). In contrast, for the smallest rods with diameters spanning 100–400 nm, 64-nm filaments began to align along the long axis (axis of zero curvature) of the rod to avoid the higher positive curvature (Fig. 2 E). For longer filaments, this alignment is even more evident (Fig. 2, E and G, pink and blue boxes). These data suggest even short septin filaments align along positive curvature.

We predicted that with longer septin filaments and/or lateral interactions, a tighter distribution of orientations would be seen. Indeed, on narrow- and wide-diameter rods (Fig. 3 E, pink and blue) with septins at high concentrations (50–500 nM) filaments are well aligned with one another and tightly packed. On rod diameters from ∼400 nm through ∼630 nm, septin filaments exhibit a wide range of orientations (Fig. 3 E; yellow). However, neighboring filaments have a tendency to align with one another. Septin filament orientation is very similar on other lipid compositions, including dioleoyl-PS (DOPS), dioleoyl-phosphoethananolamine (DOPE), and phosphatidylinositol (PI)-4,5-bis-phosphate ($PI[_{4,5}]P_2$), showing that septins can sense curved membranes on a variety of lipid compositions (Fig. S2). Thus, at high density, septin filaments more closely match the curvature of the rod than septin filaments at a low density.

These data suggest that the ability of septins to perceive micrometer-scale curvature may be in part driven by septin filament density and filament length. Both length and packing may contribute to the cooperativity detected in the saturation binding curves (Fig. 1 B). Aligned septin filaments in close proximity to each other might be stabilized by lateral interactions with one another as has been noted previously (Fig. 3 D; Frazier et al., 1998; Bertin et al., 2008; Sadian et al., 2013). We also imagine that tightly packed septins might sterically hinder one another, thus "enforcing" alignment along the optimal curvature through transient interactions while diffusing on the membrane. At higher septin concentrations, filaments are also longer on rods than at

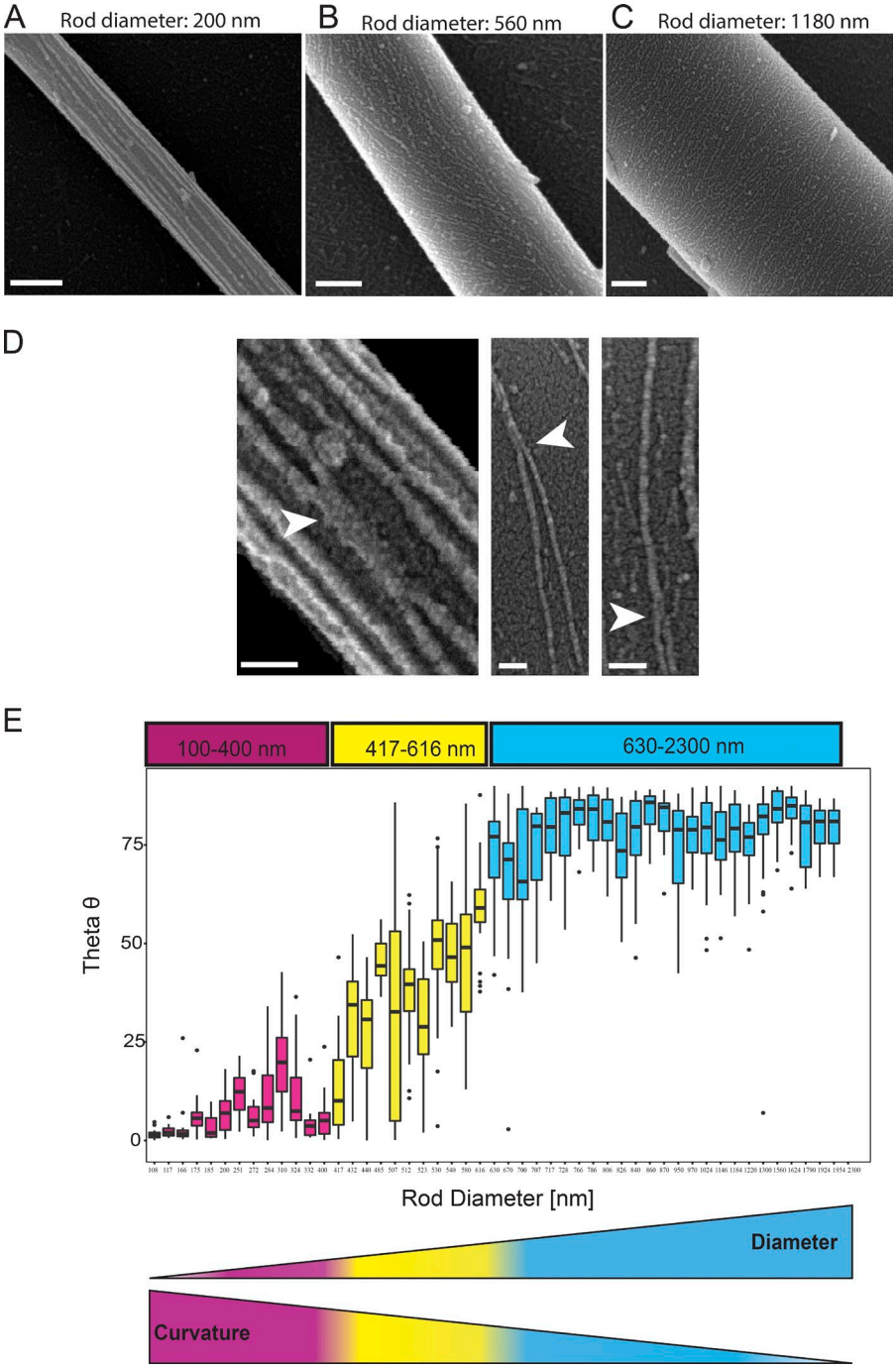

Figure 3. **Septin filament orientation is dependent on membrane curvature.** SLBs (75% DOPC, 25% PI, and trace Rh-PE) were generated on borosilicate rods of different diameters (100–2,300 nm). Purified septins were added to SLBs at saturating concentrations (from 50 nM to 500 nM) and imaged using scanning EM. **(A–C)** Representative images of septin filament alignment on rods from the three different categories at 50 nM septin concentration. Bar, 200 nm. **(D)** Example septin bundling (white arrowheads). Bar, 50 nm. **(E)** Box and whisker plots of septin filament orientation on measured rod diameters at several septin concentrations (50 nM, 100 nM, 250 nM, and 500 nM). The number of filament orientations measured per rod ranged >10 filaments. Quantification is from 49 rods. Measured filaments were >100 nm (~3 octamers) in length. Black bars represent the median. Error bars are standard deviations.

low concentrations, so it is possible that filament length is also a driving factor in this assay.

Association rates of single septin complex are curvature sensitive

We next examined curvature-dependent septin affinity differences. We measured the number and duration of binding events to calculate association and off rates for single septin complexes on curvatures of 2 μm^{-1} and 0.67 μm^{-1} (Fig. 4 and Fig. S1). Histograms of dwell times for single septin complex–binding events were fit to a single exponential decay function. The measured dwell times for these curvatures were 0.21s ± 0.019 and 0.21 ± 0.023 for $\kappa = 2\ \mu m^{-1}$ and $\kappa = 0.67\ \mu m^{-1}$, respectively ($N_{particles\ per\ curvature} > 150$). Dwell times correspond to a high off-rate, supporting previous observations that a single septin octamer does not stably associate with membranes (Bridges et al., 2016). Notably, the measured dwell times were the same on both curvatures tested, suggesting that curvature does not influence the off rate. Next, association rates were quantified by calculating the number of binding events over the product of septin concentration, time, and binding area. We found that single septin octamers show differences in the association rate as a function of membrane curvature (Fig. 4; $\kappa = 2\ \mu m^{-1}$ was 0.061 $\mu m^{-2}\ s^{-1}\ nM^{-1}$ and $\kappa = 0.67\ \mu m^{-1}$ was 0.025 $\mu m^{-2}\ s^{-1}\ nM^{-1}$).

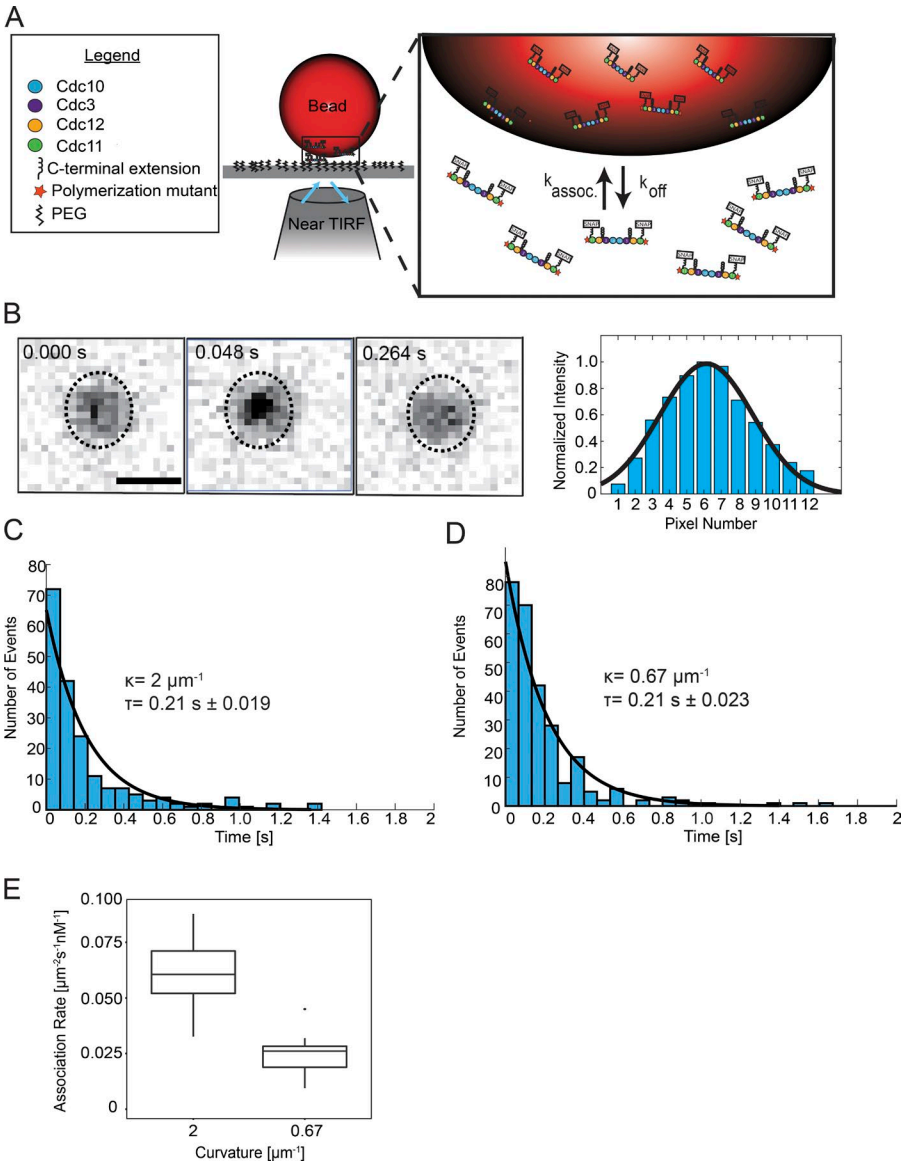

Figure 4. **Single septin complexes have a higher association rate for optimal membrane curvatures. (A)** SLBs (75% DOPC and 25% PI) were reconstituted on curvatures of 2 μm^{-1} or 0.67 μm^{-1} and flowed between two PEG (black)-coated coverslips (top coverslip not shown). Nonpolymerizable septin complexes were then flowed into the chamber, and septin binding and unbinding events were observed using near-total internal reflection fluorescence microscopy. **(B)** Representative images of a binding event on κ= 2 μm^{-1} (1 μm bead). Line scan through the particle shows signal intensity fit to a Gaussian function. **(C and D)** Dwell time histograms for membrane curvature of 2 μm^{-1} and 0.67 μm^{-1}, respectively. **(E)** Box and whisker plot quantifying association rate of nonpolymerizable septin complexes onto both curvatures (κ =2 μm^{-1} and 0.67 μm^{-1}). Black bars represent the median. Error bars are standard deviations. N_{beads} = 10 (for κ =2 μm^{-1} and 0.67 μm^{-1}); $N_{binding\ events}$ = 844 and 315 for for κ = 2 μm^{-1} and 0.67 μm^{-1}, respectively.

The ∼2.5-fold difference in association rate between these two curvatures was striking, given that our saturation binding isotherms show K_d values so close to one another (13.5 and 18.5 nM, respectively). This could be explained by the fact that our binding curve data are a summation of several reactions: initial binding, septin annealing and fragmentation events, and lateral interactions, all of which may be influenced by curvature and contribute to the K_d values. These results suggest that even a single septin octamer can detect curvature differences through the initial association with the curved membrane, and curvature-dependent bilayer defects are perceptible on micrometer-scale curvature.

An AH domain in septins is necessary and sufficient for curvature sensing

How can the association rate of a single septin octamer be sensitive to curvature on the micrometer scale? Many proteins that sense nanometer scale curvatures contain membrane-binding AHs (Drin et al., 2007; Drin and Antonny, 2010). Interestingly, another micrometer-scale curvature sensor, SpoVM, a 26–amino acid polypeptide, utilizes an 11-residue AH to sense curvature (Gill et al., 2015) and also shows curvature-dependent association rates (Kim et al., 2017). We manually searched for AH motifs in septin sequences using Heliquest (Gautier et al., 2008) to screen primary sequences for α-helical properties and found conserved, predicted AHs at the C-termini of a subset of septins (Fig. 5). Despite differences in amino acid composition, septin AH motifs are similarly situated within the primary sequence and have similar lengths, net charges, and hydrophobic moments, suggesting that the physicochemical properties of the AH domains are highly conserved across multiple species (Fig. S3).

We asked if the septin AH domain confers specificity for curved membranes. Interestingly, the AH domain of Cdc12 is truncated in a well-characterized, temperature-sensitive septin mutant, *cdc12-6* (Fig. 5; Adams and Pringle, 1984; Johnson et al., 2015). In these mutants, septins localize normally to the bud neck at permissive temperature, but rapidly disassemble at restrictive temperature (Gladfelter et al., 2005). First, we evaluated whether the AH was necessary for curvature sensing using recombinant

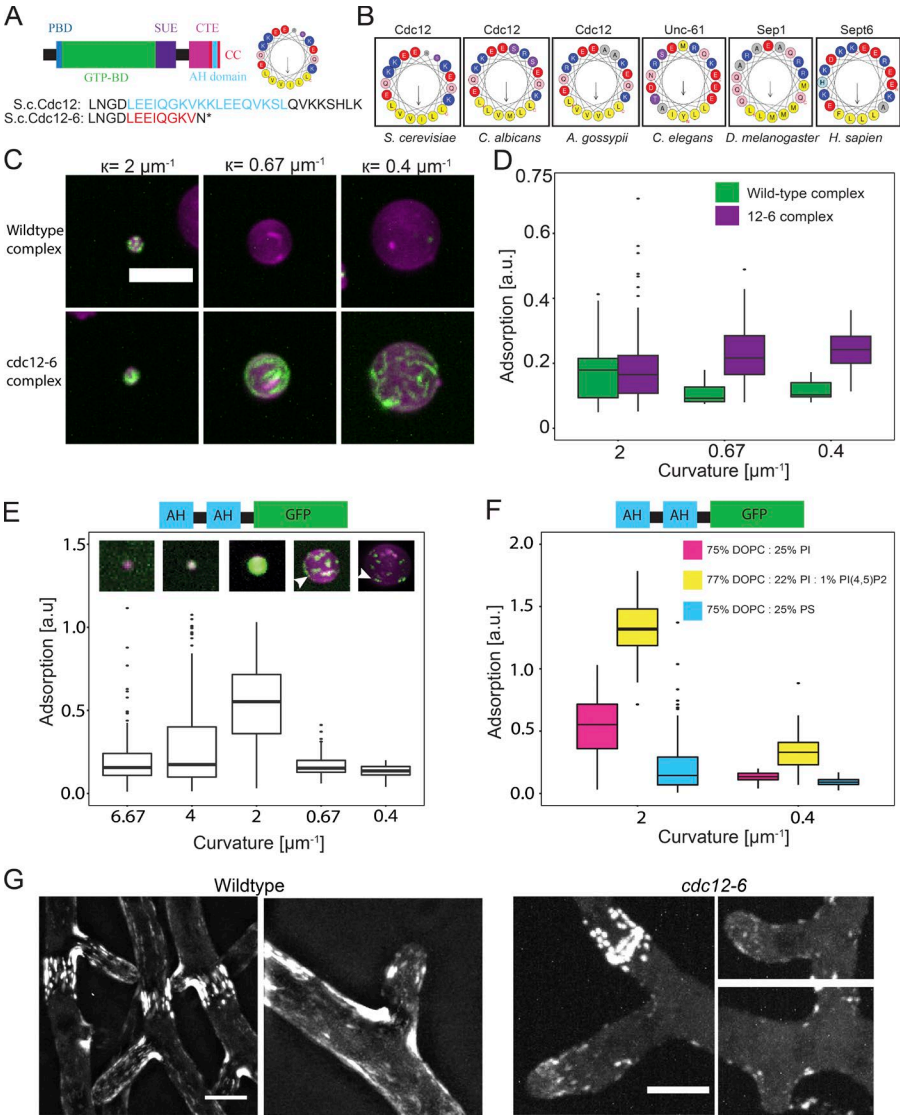

Figure 5. **Septins have conserved AHs at their C-termini. (A)** Domains within the yeast septin, Cdc12. PBD (blue): polybasic domain; GTP-BD (green): GTP-binding domain; SUE (purple): Septin unique element; CTE (pink): C-terminal extension; CC (magenta): coiled-coil domain (red); AH domain (cyan). The AH domain is shown as a helical wheel, corresponding primary sequences for WT Cdc12 and Cdc12-6 (below). **(B)** AHs found in the C-terminal extensions of septins in multiple species represented through helical wheel diagrams. **(C)** 1 nM purified WT septin complexes and *cdc12-6* septin complexes adsorption (green) onto SLBs (magenta) with different curvatures. Bar, 5 µm. **(D)** Box and whisker plot quantifying adsorption of WT or cdc12-6 septin complexes onto SLBs of various curvature. Black bars represent the median. Error bars represent the standard deviation. $n > 50$ beads for each curvature. **(E)** Representative images of 1 µM 2×-Cdc12 AH-GFP binding onto SLBs on beads with curvatures. Arrows highlight filament-like structures. **(F)** Box and whisker plot of 2×-Cdc12 AH-GFP adsorption onto different membrane compositions and curvatures. Black bars represent the median. Error bars at each curvature are standard deviations for $n > 100$ beads. **(G)** Septins assemble at the base hyphal branches in WT cells (Cdc11a-GFP), but rarely assemble in *cdc12-6* mutants (cdc12-6-GFP) at permissive temperature. Bar, 5 µm.

septin complex with the Cdc12-6 protein. Interestingly, we found that Cdc12-6 mutant complexes bound all tested membrane curvatures indiscriminately in contrast to WT septins (Fig. 5, C and D). This suggests that AH of Cdc12 is not required for septin membrane association, but rather it specifies septin preference for membrane curvature.

Next, we asked if the AH of Cdc12 was sufficient to distinguish membrane curvature. We purified a polypeptide with two copies of the AH to mimic the stoichiometry of the intact septin complex, which has two copies of Cdc12. This tandem AH polypeptide adsorbed onto membrane curvatures of 2 μm^{-1} (albeit significantly less than septin complexes), while showing reduced binding to other tested membrane curvatures of 6.67, 4, 0.67, and 0.4 μm^{-1} (Fig. 5 E). The reduced binding onto beads of $\kappa = 0.67\ \mu m^{-1}$ was surprising, given the robust binding of septin complexes to this curvature (Fig. 1). We suspect that the spacing between tandem AH domains is an important factor in tuning the curvature preference as the spacing between AH domains in this construct is only nine amino acids, whereas the spacing within a septin complex is ~24 nm (Bertin et al., 2008). Interestingly, a single AH-GFP adsorbed onto a range of more highly curved surfaces (κ = 6.67, 4, and 2 μm^{-1}) but less so on shallower curvatures (κ = 0.67 and 0.4 μm^{-1}; Fig. S2). However, we observed filament-like structures forming within both 2× AH-GFP and 1× AH-GFP constructs (Fig. 5 E and Fig. S2 K, white arrowheads), suggesting that AH domains are capable of oligomerizing at the membrane. We speculate that oligomerization of AH domains might be important for specifying preference for membrane curvature, which might be expected, given the small size of the domains (Huang and Ramamurthi, 2010). We see identical behavior with a tandem construct lacking a GFP tag and visualized by dye labeling showing that the preference and any oligomerization is not an artifact of the tag (unpublished data). Collectively, this data suggests that the spatial arrangement of AH domains and the capacity to self-assemble likely tune curvature sensitivity.

There is strong evidence that AH domains demonstrate lipid-specific binding (Vanni et al., 2014; Hofbauer et al., 2018). Similarly, septins preferentially bind membranes containing $PI_{(4,5)}P_2$, which may be dependent on the presence of polybasic regions within individual septin polypeptides (Casamayor and Snyder, 2003; Akil et al., 2016). However, the polybasic motifs are potentially buried within a septin oligomer (Sirajuddin et

al., 2007; Bertin et al., 2010), and mutations within these regions could affect the assembly of septins into octamers and/or filaments and have downstream consequences that potentially impact septin–membrane interactions. We probed the AH domain lipid specificity by measuring adsorption onto both optimum ($\kappa = 2\ \mu m^{-1}$) and nonoptimum ($\kappa = 0.4\ \mu m^{-1}$) membrane curvatures with varying lipid compositions, while keeping the global charge across the membrane equivalent. There are local differences in charge of the lipids used, with $PI_{(4,5)}P_2$ (−3 at pH 7.4) being more anionic than phosphoinositol (PI) and phosphoserine (PS; both −1 at pH 7.4; Tsui et al., 1986; Beber et al., 2018). We found that curvature sensitivity remained intact on the different lipids; however, we observed increased binding of the 2× AH domain, the single AH-GFP, and the full septin complex to $PI_{(4,5)}P_2$-containing membranes over membranes containing either PI or PS (Fig. 5 F and Fig. S2, K–N). Interestingly, we observed stronger binding of the 2× AH to PI over PS, despite their equal charge, suggesting that either the molecular shape of the lipid or the different fatty acyl chain environment influences AH adsorption.

Finally, we assessed the functionality of the Cdc12 AH in live cells using *Ashbya gossypii*, a filamentous fungus which displays prominent septin assemblies at sites of micrometer-scale curvature (DeMay et al., 2009; Bridges et al., 2016). We generated a *cdc12-6* mutant allele in *A. gossypii*, similar to the *S. cerevisiae* allele. In *cdc12-6* mutants, septins rarely assemble at branches (17%; $n = 104$ branches; 12 cells), but still assembled into tightly bundled filaments, septation site rings, and thin filaments at hyphal tips (Fig. 5 G). The few branch assemblies detected were aberrant, with low signal intensity and only at the base of newly formed branches. This shows that the AH in Cdc12 is required for septin localization at curved membranes in cells.

Conclusion

We identify a mechanism that uses both affinity and the number of available binding sites to drive cooperative, curvature-specific accumulation of septins. Even a single-septin octamer is capable of detecting changes micrometer scale curvatures, manifested as differences in association rate. An AH located at the very C-terminus of Cdc12 is necessary and sufficient for septins to distinguish different lipid compositions and curvatures. It is now clear that AH domains are not just useful for sensing nanometer-scale curvature but also to detect micrometer-scale curvature. The ability of septins to bind membranes in the absence of the AH domain suggests that there are additional curvature-independent septin–membrane interaction motifs. What septin AHs sense in the local lipid environment will be an exciting area of future investigation.

Materials and methods

Yeast septin purification

BL21 (DE3) *Escherichia coli* cells were transformed using a duet expression system (Bridges et al., 2016) and selected with ampicillin and chloramphenicol. Selected cells were cultured to an $OD_{600\ nm}$ between 0.6 and 0.8 and induced with 1 mM isopropyl β-D-1-thiogalactopyranoside. Induced cultures were grown for 24 h at 22°C (3 h for Cdc12 AH construct) before harvesting. Cultures were pelleted at 10,000 relative centrifugal force (RCF) for 15 min. Pellets were resuspended in lysis buffer (1 M KCl, 50 mM, Hepes, pH 7.4, 1 mM $MgCl_2$, 10% glycerol, 1% Tween-20, and 1× protease inhibitor tablet [Roche], 20 mM Imidazole, and 1 mg/ml lysozyme) for 30 min on ice with intermittent vortexing. The lysate was sonicated twice for 10 s and clarified by centrifugation using an SS-34 rotor at 20,000 RPM for 30 min. Clarified supernatant was filtered using a 0.44-µm filter and then incubated with equilibrated Ni-NTA^{2+} or cobalt resin (Thermo Fisher Scientific; 2 ml resin per liter of *E. coli* culture) at 4°C for 1 h. Resin and lysate were added to a gravity flow column. Bound protein was washed four times with five times the column volume with wash buffer (1 M KCl, 50 mM Hepes, pH 7.4, and 20 mM Imidazole) and then eluted in elution buffer (300 mM KCl, 50 mM Hepes, pH 7.4, and 500 mM Imidazole). Eluted protein was then dialyzed into septin storage buffer (300 mM KCl, 50 mM Hepes, pH 7.4, and 1 mM β-mercaptoethanol) for 24 h in two steps (Slide-A-Lyzer G2; 20,000 molecular weight cut-off [Thermo Fisher Scientific]; 10,000 molecular weight cut-off for AH constructs). During dialysis, 60 µg of Tobacco etch virus protease (Sigma) was added to cleave the 6×-histidine tag on Cdc12. 24 h later, the protein was run over a second column (either Ni-NTA or cobalt resin) to remove the protease, the poly-histidine tag, and additional contaminants. Protein purity was determined via SDS-PAGE, and protein concentration was determined via Bradford assay. Purification of the Cdc12-6 complexes and AH domain constructs were purified as described above. However, for AH domain purifications, cells were induced for 4 h at 37°C and harvested for protein purification.

AH construct sequences

2× AH-GFP construct has the following sequence followed by a GFP tag: LEEIQGKVKKLEEQVKSL-GSGSRSGSGS-LEEIQGKVKKLEEQVKSL-GSGSSR-GFP tag, where the underlined sequences are the AH domains within Cdc12, and the serine-glycine repeats constitute the linker regions between tandem AH domains and the GFP tag. Similarly, the 1× AH construct has the following sequence: LEEIQGKVKKLEEQVKSL-GSGSSR-GFP tag.

Lipid mix preparation

All septin binding experiments were done using SLBs, consisting of 75 mole percent dioleoylphosphatidylcholine (DOPC) Avanti Polar Lipids, 25 mole percent PI (liver, bovine) sodium salt, and trace amounts (<0.1%) of phosphatidylethanolamine-N-(lissamine rhodamine B sulfonyl) (Rh-PE; ammonium salt; egg-transphosphatidylated, chicken; Avanti Polar Lipids 810146), unless otherwise mentioned. All lipid compositions were made the same way. Lipids were mixed in chloroform solvent, and dried by a stream of argon gas to generate a lipid film. Remaining solvent was evaporated by placing the lipid film under a vacuum for at least 6 h. Lipids were rehydrated in SLB buffer (300 mM KCl, 20 mM Hepes pH 7.4, and 1 mM $MgCl_2$) for 30 min at 37°C to give a final concentration of 5 mM. Hydrated lipids were subject to vortex for 10 s, every 5 min for 30 min bath sonicated in 2-min intervals until clarification to yield small unilamellar vesicles (SUVs).

Preparation of SLBs on silica microspheres

SUVs were adsorbed onto silica microspheres (Bridges et al.) of various curvatures by mixing 50 nM lipids with 440 μm^2 of silica microsphere surface area or 10 µl of rods in a final volume of 80 µl for 1 h on a roller drum at room temperature. Unbound lipid was washed away by pelleting lipid-coated beads at the minimum force required to pellet each bead size. For κ= 0.5 μm^{-1}, spin at 4.5 k RCF; κ= 2 μm^{-1}, spin at 2.3 k RCF; κ= 0.67 μm^{-1}, spin at 800 RCF; and κ=0.4 μm^{-1} spin at 300 RCF. Beads were then washed using prereaction buffer (33.3 mM KCl and 50 mM Hepes, pH 7.4). Washes were preformed four times.

Measuring protein adsorption onto silica microspheres

To examine septin adsorption onto different membrane curvatures, 25 µl of septins in septin storage buffer was added to 75 µl of a bead-buffer solution of 5 mm^2 total lipid-bead surface area to give a final buffer composition of 100 mM KCl, 50 mM Hepes, pH 7.4, 1 mM BME, 0.1% methylcellulose, and 0.1% bovine serum albumin (fatty acid free; Sigma). Saturation binding curves were obtained using several different septin concentrations in simple mixtures, containing only one bead size per reaction volume. AH adsorption was measured in mixtures containing protein and various bead diameters. Each reaction was incubated in a plastic chamber (Bridges and Gladfelter, 2016) glued to a polyethyleneglycol (PEG)–passivated coverslip for 1 h (to allow the reaction to reach equilibrium). Beads were imaged using either a wide-field microscope with a Ti-82 Nikon stage a 100× Plan Apo 1.49 NA oil lens and Zyla sCMOS (Andor; saturation binding curves) or a spinning disc (Yokogawa) confocal microscope (Nikon Ti-82 stage) using a 100× Plan Apo 1.49 NA oil lens and a Prime 95B CMOS (Photometrics; AH and Cdc12-6 septin complex adsorption experiments). For analysis of septin binding, raw images were exported into Imaris 8.1.2 (Bitplane AG). Each image was background subtracted in both channels using the software's Gaussian filter for background determination (width, 31.4 µm). The surface of each bead was defined using the lipid channel. Using the surface generate on each bead, sum intensity values from lipid and septin channels were exported from Imaris into Microsoft Excel. Septin adsorption was calculated by dividing the multiple sum intensity values from the septin channel over the sum intensity values from the lipid channel as to control for surface area for each bead size. Boxplots were generated through exporting intensity sum values from both channels into R version 3.2. 2 (R Foundation for Statistical Computing; using RStudio 0.99.467). Boxplots were generated using ggplot2 package (Wickham, 2007, 2015).

Generation and preparation of septin-rod SLB mixture

Borosilicate rods were obtained from glass microfiber filters (GFC, 42.5 mm; Whatman). A single filter was torn up into small pieces into a beaker with 60 ml of 100% ethanol and sonicated until the solution became opaque. The solution was stored at room temperature overnight. The next day, 10 µl of rods was taken from the solution after thorough mixing. 70 µl of SLB buffer was added to the rods and spun down at top speed to dilute the ethanol in the solution. This step was repeated four additional times. 5 mM SUVs (75% DOPC, 25% PI, and trace Rh-PE, as described above) were added to the polycarbonate rods and allowed to incubate for 1 h at room temperature. Unbound lipid was washed away, pelleting lipid-coated beads at top speed (16.1 RCF) using prereaction buffer. The mixture of septin-lipid–coated rods was added to circular 12-mm PEG-coated coverslips and incubated at room temperature for 1 h and then prepared for scanning EM.

Scanning EM

The septin–rod mixture was addedonto a circular PEG-coated 12-mm coverslip and was fixed in 2.5% glutaraldehyde in 0.05 M sodium cacodylate (NaCo), pH 7.4, for 30 min, followed by two washes in 0.05 M NaCo (5 min each wash). Samples were post-fixed in 0.5% OsO_4 cacodylate buffer for 30 min and washed three times in NaCo (5 min each wash). Samples were then incubated with 1% tannic acid for 15 min, followed by three washes in NaCo. 0.5% OsO_4 was added for 15 min, followed by three washes in NaCo. Samples were then dehydrated with increasing ethanol concentrations (30% EtOH for 5 min, twice; 50% EtOH for 5 min; 75% EtOH for 5 min; and 100% EtOH for 5 min, twice followed by another 10 min incubation). Samples were incubated in transition fluid (hexamethyldisilazane) three times (incubation times: 5 min, 10 min, and 5 min), allowed to air dry, and then placed in a desiccator until sputter coating. Samples were coated in a gold/palladium alloy and then imaged on a Zeiss Supra 25 Field Emission scanning electron microscope.

Kinetics of single septin complex onto lipid-coated beads

Two PEG-passivated coverslips were sandwiched together using double-coated, pressure-sensitive adhesive tape (Nitto product: 5015ELE) to make narrow (~20 µl) flow chambers. A mixture of septins and lipid-coated beads of a given diameter were then flowed through the chamber and imaged using near-total internal reflection fluorescence microscopy. The number and duration of binding events were performed manually. Association rate was quantified by calculating the number of binding events over the product of septin concentration, time, and binding area. To ensure the off-rates were not dominated by bleaching, we generated bleach profiles (Fig. S1). The amount of time it took to bleach single septin complexes is much higher than the observed dwell time (~1.5 s). Bleach steps were also used to calibrate intensity so that scored puncta were single septin complexes. As a control, we measured the dwell time of single septin molecules that localized to areas of the coverslip that did not contain any beads, and wemeasured a dwell time of 0.062 s (unpublished data), ensuring that our measured dwell times on beads reflect accurate association dynamics of single septin molecules on lipid-coated beads.

Generation of helical wheel diagrams

Helical wheels and the calculation of net charge and hydrophobic moment were generated using Heliquest (Gautier et al., 2008).

A. gossypii strain construction, culture, and imaging

We generated an analogous *cdc12-6* allele (LEEVQAKVKKLEEQV RALQLRKH* → LEEVQAKVKN*) with GFP tag for integration at the endogenous locus by cloning a FragmentGENE (Genewiz; 637

bp), harboring the mutation into AGB260 (*pCDC12*-GFP:*GEN*; Meseroll et al., 2013) via the restriction enzymes *BspEI* and *BsrGI*, yielding AGB1209 (*pcdc12-6*-GFP:*GEN*). AGB1209 was linearized by digestion with *SphI* for targeted integration at the *CDC12* locus and transformed into the WT *A. gossypii* strain (Altmann-Jöhl and Philippsen, 1996) to generate AG884 (*Agcdc12-6*-GFP:GEN *leu2Δ thr4Δ*). AG384 (*AgCDC11a*-GFP:*GEN leu2Δ thr4Δ*) is described in Meseroll et al. (2013).

A. gossypii strains were grown from spores in full medium at either 24°C (*cdc12-6*) for 24 h or 30°C (WT) for 16 h before harvesting mycelial cells. Cells were mounted onto Low Fluorescence medium pads solidified with 2% agarose for imaging. Images were acquired using a spinning disc (Yokogawa) confocal microscope (Nikon Ti-82 stage) using a 100× Plan Apo 1.49 NA oil lens and a Prime 95B CMOS (Photometrics).

Online supplemental material

Fig. S1 shows single molecule-binding and -unbinding events and successful purification of multiple proteins used in this study. Fig. S2 shows the arrangement of septin filaments on a range of membrane curvatures using different lipid compositions. It also shows the binding profiles of 1 and 2× AH-GFP and whole septin complex-binding to different membrane curvatures using different lipid compositions. Fig. S3 shows the physiochemical properties of both septin and nonseptin AH domains. Table S1 shows the biochemical parameters for septin adsorption onto various membrane curvatures. Table S2 shows the coefficient of variation for septin filament alignment on rods.

Acknowledgments

We thank the Gladfelter laboratory and Danny Lew for useful discussions, Matthias Garten for ideas in setting up the rod assay, and the University of North Carolina EM facility (Victoria Madden and Kristen White) for support with scanning electron microscope.

This work was supported by a Howard Hughes Medical Institute Faculty Scholars award to A.S. Gladfelter, and K.S. Cannon was supported in part by a grant from the National Institute of General Medical Sciences under award T32 GM119999.

The authors declare no competing financial interests.

Author contributions: K.S. Cannon and B.L. Woods conducted experiments; B.L. Woods and J.M. Crutchley constructed strains for experiments; B.L. Woods and J.M. Crutchley constructed plasmids for experiments; K.S. Cannon, B.L. Woods, and A.S. Gladfelter designed experiments.

Submitted: 27 July 2018
Revised: 17 November 2018
Accepted: 7 January 2019

References

Adams, A.E.M., and J.R. Pringle. 1984. Relationship of actin and tubulin distribution to bud growth in wild-type and morphogenetic-mutant Saccharomyces cerevisiae. *J. Cell Biol.* 98:934–945. https://doi.org/10.1083/jcb.98.3.934

Akil, A., J. Peng, M. Omrane, C. Gondeau, C. Desterke, M. Marin, H. Tronchère, C. Taveneau, S. Sar, P. Briolotti, et al. 2016. Septin 9 induces lipid droplets growth by a phosphatidylinositol-5-phosphate and microtubule-dependent mechanism hijacked by HCV. *Nat. Commun.* 7:12203. https://doi.org/10.1038/ncomms12203

Altmann-Jöhl, R., and P. Philippsen. 1996. AgTHR4, a new selection marker for transformation of the filamentous fungus Ashbya gossypii, maps in a four-gene cluster that is conserved between A. gossypii and Saccharomyces cerevisiae. *Mol. Gen. Genet.* 250:69–80. https://doi.org/10.1007/BF02191826

Beber, A., M. Alqabandi, C. Prévost, F. Viars, D. Lévy, P. Bassereau, A. Bertin, and S. Mangenot. 2018. Septin-based readout of PI(4,5)P2 incorporation into membranes of giant unilamellar vesicles. *Cytoskeleton (Hoboken)*. https://doi.org/10.1002/cm.21480

Bertin, A., M.A. McMurray, P. Grob, S.-S. Park, G. Garcia III, I. Patanwala, H.-L. Ng, T. Alber, J. Thorner, and E. Nogales. 2008. Saccharomyces cerevisiae septins: supramolecular organization of heterooligomers and the mechanism of filament assembly. *Proc. Natl. Acad. Sci. USA.* 105:8274–8279. https://doi.org/10.1073/pnas.0803330105

Bertin, A., M.A. McMurray, L. Thai, G. Garcia III, V. Votin, P. Grob, T. Allyn, J. Thorner, and E. Nogales. 2010. Phosphatidylinositol-4,5-bisphosphate promotes budding yeast septin filament assembly and organization. *J. Mol. Biol.* 404:711–731. https://doi.org/10.1016/j.jmb.2010.10.002

Bridges, A., and A. Gladfelter. 2016. Chapter 4 - In vitro reconstitution of septin assemblies on supported lipid bilayers. *Methods in Cell Biology*. 136:57–71. https://doi.org/10.1016/bs.mcb.2016.03.025

Bridges, A.A., M.S. Jentzsch, P.W. Oakes, P. Occhipinti, and A.S. Gladfelter. 2016. Micron-scale plasma membrane curvature is recognized by the septin cytoskeleton. *J. Cell Biol.* 213:23–32. https://doi.org/10.1083/jcb.201512029

Byers, B., and L. Goetsch. 1976. A highly ordered ring of membrane-associated filaments in budding yeast. *J. Cell Biol.* 69:717–721. https://doi.org/10.1083/jcb.69.3.717

Cannon, K.S., B.L. Woods, and A.S. Gladfelter. 2017. The Unsolved Problem of How Cells Sense Micron-Scale Curvature. *Trends Biochem. Sci.* 42:961–976. https://doi.org/10.1016/j.tibs.2017.10.001

Casamayor, A., and M. Snyder. 2003. Molecular dissection of a yeast septin: distinct domains are required for septin interaction, localization, and function. *Mol. Cell. Biol.* 23:2762–2777. https://doi.org/10.1128/MCB.23.8.2762-2777.2003

Cho, S.J., H. Lee, S. Dutta, J. Song, R. Walikonis, and I.S. Moon. 2011. Septin 6 regulates the cytoarchitecture of neurons through localization at dendritic branch points and bases of protrusions. *Mol. Cells.* 32:89–98. https://doi.org/10.1007/s10059-011-1048-9

Clay, L., F. Caudron, A. Denoth-Lippuner, B. Boettcher, S. Buvelot Frei, E.L. Snapp, and Y. Barral. 2014. A sphingolipid-dependent diffusion barrier confines ER stress to the yeast mother cell. *eLife.* 3:e01883. https://doi.org/10.7554/eLife.01883

DeMay, B.S., R.A. Meseroll, P. Occhipinti, and A.S. Gladfelter. 2009. Regulation of distinct septin rings in a single cell by Elm1p and Gin4p kinases. *Mol. Biol. Cell.* 20:2311–2326. https://doi.org/10.1091/mbc.e08-12-1169

Drin, G., and B. Antonny. 2010. Amphipathic helices and membrane curvature. *FEBS Lett.* 584:1840–1847. https://doi.org/10.1016/j.febslet.2009.10.022

Drin, G., J.F. Casella, R. Gautier, T. Boehmer, T.U. Schwartz, and B. Antonny. 2007. A general amphipathic α-helical motif for sensing membrane curvature. *Nat. Struct. Mol. Biol.* 14:138–146. https://doi.org/10.1038/nsmb1194

Field, C.M., O. al-Awar, J. Rosenblatt, M.L. Wong, B. Alberts, and T.J. Mitchison. 1996. A purified Drosophila septin complex forms filaments and exhibits GTPase activity. *J. Cell Biol.* 133:605–616. https://doi.org/10.1083/jcb.133.3.605

Finnigan, G.C., E.A. Booth, A. Duvalyan, E.N. Liao, and J. Thorner. 2015. The carboxy-terminal tails of septins Cdc11 and Shs1 recruit myosin-II binding factor Bni5 to the bud neck in Saccharomyces cerevisiae. *Genetics.* 200:843–862. https://doi.org/10.1534/genetics.115.176503

Ford, S.K., and J.R. Pringle. 1991. Cellular morphogenesis in the Saccharomyces cerevisiae cell cycle: localization of the CDC11 gene product and the timing of events at the budding site. *Dev. Genet.* 12:281–292. https://doi.org/10.1002/dvg.1020120405

Frazier, J.A., M.L. Wong, M.S. Longtine, J.R. Pringle, M. Mann, T.J. Mitchison, and C. Field. 1998. Polymerization of purified yeast septins: evidence

that organized filament arrays may not be required for septin function. *J. Cell Biol.* 143:737–749. https://doi.org/10.1083/jcb.143.3.737

Garcia, G. III, A. Bertin, Z. Li, Y. Song, M.A. McMurray, J. Thorner, and E. Nogales. 2011. Subunit-dependent modulation of septin assembly: budding yeast septin Shs1 promotes ring and gauze formation. *J. Cell Biol.* 195:993–1004. https://doi.org/10.1083/jcb.201107123

Gautier, R., D. Douguet, B. Antonny, and G. Drin. 2008. HELIQUEST: a web server to screen sequences with specific α-helical properties. *Bioinformatics.* 24:2101–2102. https://doi.org/10.1093/bioinformatics/btn392

Gill, R.L. Jr., J.P. Castaing, J. Hsin, I.S. Tan, X. Wang, K.C. Huang, F. Tian, and K.S. Ramamurthi. 2015. Structural basis for the geometry-driven localization of a small protein. *Proc. Natl. Acad. Sci. USA.* 112:E1908–E1915. https://doi.org/10.1073/pnas.1423868112

Gladfelter, A.S., L. Kozubowski, T.R. Zyla, and D.J. Lew. 2005. Interplay between septin organization, cell cycle and cell shape in yeast. *J. Cell Sci.* 118:1617–1628. https://doi.org/10.1242/jcs.02286

Gopalakrishnan, G., I. Rouiller, D.R. Colman, and R.B. Lennox. 2009. Supported bilayers formed from different phospholipids on spherical silica substrates. *Langmuir.* 25:5455–5458. https://doi.org/10.1021/la9006982

Haarer, B.K., and J.R. Pringle. 1987. Immunofluorescence localization of the Saccharomyces cerevisiae CDC12 gene product to the vicinity of the 10-nm filaments in the mother-bud neck. *Mol. Cell. Biol.* 7:3678–3687. https://doi.org/10.1128/MCB.7.10.3678

Hatzakis, N.S., V.K. Bhatia, J. Larsen, K.L. Madsen, P.Y. Bolinger, A.H. Kunding, J. Castillo, U. Gether, P. Hedegård, and D. Stamou. 2009. How curved membranes recruit amphipathic helices and protein anchoring motifs. *Nat. Chem. Biol.* 5:835–841. https://doi.org/10.1038/nchembio.213

Hofbauer, H.F., M. Gecht, S.C. Fischer, A. Seybert, A.S. Frangakis, E.H.K. Stelzer, R. Covino, G. Hummer, and R. Ernst. 2018. The molecular recognition of phosphatidic acid by an amphipathic helix in Opi1. *J. Cell Biol.* 217:3109–3126. https://doi.org/10.1083/jcb.201802027

Huang, K.C., and K.S. Ramamurthi. 2010. Macromolecules that prefer their membranes curvy. *Mol. Microbiol.* 76:822–832. https://doi.org/10.1111/j.1365-2958.2010.07168.x

Hussain, S., C.N. Wivagg, P. Szwedziak, F. Wong, K. Schaefer, T. Izoré, L.D. Renner, M.J. Holmes, Y. Sun, A.W. Bisson-Filho, et al. 2018. MreB filaments align along greatest principal membrane curvature to orient cell wall synthesis. *eLife.* 7:e32471. https://doi.org/10.7554/eLife.32471

John, C.M., R.K. Hite, C.S. Weirich, D.J. Fitzgerald, H. Jawhari, M. Faty, D. Schläpfer, R. Kroschewski, F.K. Winkler, T. Walz, et al. 2007. The Caenorhabditis elegans septin complex is nonpolar. *EMBO J.* 26:3296–3307. https://doi.org/10.1038/sj.emboj.7601775

Johnson, C.R., A.D. Weems, J.M. Brewer, J. Thorner, and M.A. McMurray. 2015. Cytosolic chaperones mediate quality control of higher-order septin assembly in budding yeast. *Mol. Biol. Cell.* 26:1323–1344. https://doi.org/10.1091/mbc.E14-11-1531

Joo, E., M.C. Surka, and W.S. Trimble. 2007. Mammalian SEPT2 is required for scaffolding nonmuscle myosin II and its kinases. *Dev. Cell.* 13:677–690. https://doi.org/10.1016/j.devcel.2007.09.001

Khan, A., J. Newby, and A.S. Gladfelter. 2018. Control of septin filament flexibility and bundling by subunit composition and nucleotide interactions. *Mol. Biol. Cell.* 29:702–712. https://doi.org/10.1091/mbc.E17-10-0608

Kim, E.Y., E.R. Tyndall, K.C. Huang, F. Tian, and K.S. Ramamurthi. 2017. Dash-and-Recruit Mechanism Drives Membrane Curvature Recognition by the Small Bacterial Protein SpoVM. *Cell Syst.* 5:518–526.e3. https://doi.org/10.1016/j.cels.2017.10.004

Longtine, M.S., C.L. Theesfeld, J.N. McMillan, E. Weaver, J.R. Pringle, and D.J. Lew. 2000. Septin-dependent assembly of a cell cycle-regulatory module in Saccharomyces cerevisiae. *Mol. Cell. Biol.* 20:4049–4061. https://doi.org/10.1128/MCB.20.11.4049-4061.2000

Maddox, A.S., L. Lewellyn, A. Desai, and K. Oegema. 2007. Anillin and the septins promote asymmetric ingression of the cytokinetic furrow. *Dev. Cell.* 12:827–835. https://doi.org/10.1016/j.devcel.2007.02.018

Meitinger, F., M.E. Boehm, A. Hofmann, B. Hub, H. Zentgraf, W.D. Lehmann, and G. Pereira. 2011. Phosphorylation-dependent regulation of the F-BAR protein Hof1 during cytokinesis. *Genes Dev.* 25:875–888. https://doi.org/10.1101/gad.622411

Meseroll, R.A., P. Occhipinti, and A.S. Gladfelter. 2013. Septin phosphorylation and coiled-coil domains function in cell and septin ring morphology in the filamentous fungus Ashbya gossypii. *Eukaryot. Cell.* 12:182–193. https://doi.org/10.1128/EC.00251-12

Pan, F., R.L. Malmberg, and M. Momany. 2007. Analysis of septins across kingdoms reveals orthology and new motifs. *BMC Evol. Biol.* 7:103. https://doi.org/10.1186/1471-2148-7-103

Pranke, I.M., V. Morello, J. Bigay, K. Gibson, J.M. Verbavatz, B. Antonny, and C.L. Jackson. 2011. α-Synuclein and ALPS motifs are membrane curvature sensors whose contrasting chemistry mediates selective vesicle binding. *J. Cell Biol.* 194:89–103. https://doi.org/10.1083/jcb.201011118

Ramamurthi, K.S., S. Lecuyer, H.A. Stone, and R. Losick. 2009. Geometric cue for protein localization in a bacterium. *Science.* 323:1354–1357. https://doi.org/10.1126/science.1169218

Sadian, Y., C. Gatsogiannis, C. Patasi, O. Hofnagel, R.S. Goody, M. Farkasovský, and S. Raunser. 2013. The role of Cdc42 and Gic1 in the regulation of septin filament formation and dissociation. *eLife.* 2:e01085. https://doi.org/10.7554/eLife.01085

Sakchaisri, K., S. Asano, L.R. Yu, M.J. Shulewitz, C.J. Park, J.E. Park, Y.W. Cho, T.D. Veenstra, J. Thorner, and K.S. Lee. 2004. Coupling morphogenesis to mitotic entry. *Proc. Natl. Acad. Sci. USA.* 101:4124–4129. https://doi.org/10.1073/pnas.0400641101

Simunovic, M., A. Srivastava, and G.A. Voth. 2013. Linear aggregation of proteins on the membrane as a prelude to membrane remodeling. *Proc. Natl. Acad. Sci. USA.* 110:20396–20401. https://doi.org/10.1073/pnas.1309819110

Simunovic, M., G.A. Voth, A. Callan-Jones, and P. Bassereau. 2015. When Physics Takes Over: BAR Proteins and Membrane Curvature. *Trends Cell Biol.* 25:780–792. https://doi.org/10.1016/j.tcb.2015.09.005

Sirajuddin, M., M. Farkasovsky, F. Hauer, D. Kühlmann, I.G. Macara, M. Weyand, H. Stark, and A. Wittinghofer. 2007. Structural insight into filament formation by mammalian septins. *Nature.* 449:311–315. https://doi.org/10.1038/nature06052

Spiliotis, E.T., M. Kinoshita, and W.J. Nelson. 2005. A mitotic septin scaffold required for Mammalian chromosome congression and segregation. *Science.* 307:1781–1785. https://doi.org/10.1126/science.1106823

Tsui, F.C., D.M. Ojcius, and W.L. Hubbell. 1986. The intrinsic pKa values for phosphatidylserine and phosphatidylethanolamine in phosphatidylcholine host bilayers. *Biophys. J.* 49:459–468. https://doi.org/10.1016/S0006-3495(86)83655-4

Ursell, T.S., J. Nguyen, R.D. Monds, A. Colavin, G. Billings, N. Ouzounov, Z. Gitai, J.W. Shaevitz, and K.C. Huang. 2014. Rod-like bacterial shape is maintained by feedback between cell curvature and cytoskeletal localization. *Proc. Natl. Acad. Sci. USA.* 111:E1025–E1034. https://doi.org/10.1073/pnas.1317174111

Vanni, S., H. Hirose, H. Barelli, B. Antonny, and R. Gautier. 2014. A sub-nanometre view of how membrane curvature and composition modulate lipid packing and protein recruitment. *Nat. Commun.* 5:4916. https://doi.org/10.1038/ncomms5916

Westfall, P.J., and M. Momany. 2002. Aspergillus nidulans septin AspB plays pre- and postmitotic roles in septum, branch, and conidiophore development. *Mol. Biol. Cell.* 13:110–118. https://doi.org/10.1091/mbc.01-06-0312

Wickham, H. 2007. Reshaping Data with the reshape Package. *J. Stat. Softw.* 21:1–20. https://doi.org/10.18637/jss.v021.i12

Wickham, H. 2015. dplyr: A Grammar of Data Manipulation. R package version 0.4.3. Available at: https://dplyr.tidyverse.org (accessed November 1, 2018).

Yamada, S., T. Isogai, R. Tero, Y. Tanaka-Takiguchi, T. Ujihara, M. Kinoshita, and K. Takiguchi. 2016. Septin Interferes with the Temperature-Dependent Domain Formation and Disappearance of Lipid Bilayer Membranes. *Langmuir.* 32:12823–12832. https://doi.org/10.1021/acs.langmuir.6b03452

Zimmerberg, J., and M.M. Kozlov. 2006. How proteins produce cellular membrane curvature. *Nat. Rev. Mol. Cell Biol.* 7:9–19. https://doi.org/10.1038/nrm1784